World Scientific
www.worldscientific.com

NUCLEON RESONANCES AND QUARK STRUCTURE

J. T. LONDERGAN

Physics Dept and Nuclear Theory Center, Indiana University,
Bloomington, IN 47405, USA
tlonderg@indiana.edu

A review of the past 50 years of study of resonances, leading to our understanding of the quark content of baryons and mesons. The quark structure of the proton as revealed through deep inelastic scattering. Structure functions and what they reveal about proton structure. Prospects for further studies with new and upgraded facilities, particularly a proposed electron-ion collider.

1. Introduction

These lectures are intended for Indian graduate students and postdocs in nuclear physics, providing a pedagogical review of the past 50 years of experimental and theoretical studies of the quark and gluon structure of the nucleon. Since many speakers at this workshop will discuss structure functions extracted from deep inelastic scattering reactions, we define these quantities and review what can be extracted from them. We hope that specialists in this field will tolerate our brief summary of many years' study of strongly-interacting systems.

Fig. 1. Richard H. Dalitz, 1925-2006.

These lectures are dedicated to my mentor, Richard Dalitz, who was from 1963-2000 Royal Society Professor of Physics at Oxford University and who made seminal contributions in particle phenomenology. Dalitz pairs (electron-positron pairs from decay of a high-energy photon) and the Dalitz plot were named after him. In addition he made important contributions to our understanding of strange particles and

hypernuclei, and to particle spectroscopy through the constituent-quark model. I appreciated his insights into theoretical physics, his keen intuition about physical problems, and his encouragement of young physicists.

2. Discovery of New Particles with Dedicated Accelerators

The development of both accelerators and detectors progressed rapidly through the first half of the 20th century.[1] Ernest Lawrence's cyclotron ushered in a new era which provided both much higher beam energies and more intense beams than were previously possible. This was followed by the development of synchrotrons and mastery of magnetic focusing techniques, which allowed particles to be contained in a circular pipe surrounded by individual focusing magnets. Shortly following World War II, development began on a succession of machines based upon the synchrotron principle. Advances in accelerator technology were accompanied by corresponding advances in particle detectors. The bubble chamber was an extremely important tool in discovering new particles. In particular strange particles like the Ξ and Ω were discovered in bubble chambers. Another major detector advance was the development of the spark chamber.

Most of the particles discovered before the 1950s were either completely stable (so far as we know), like the electron or proton, or had relatively long lifetimes. For example, the lifetimes of charged pions and kaons are roughly 10^{-8} seconds, and the lifetimes of the Λ and charged Σ are of order 10^{-10} seconds. When charged (neutral) particles move with sufficiently large velocities, they leave measurable tracks (gaps) in emulsions or bubble chambers between their production and decay vertices.

Starting in the early 1950s, researchers began to discover states which were much more short-lived than these earlier particles. These states were extracted from scattering experiments at what were then the highest available energies. Fig. 2 shows elastic and total cross sections for $\pi^+ - p$ scattering. Note the very prominent peak at CM energy just near 1.2 GeV. This is what was then called the 'P_{33} resonance' in $\pi - p$ scattering. The notation for this state denoted the angular momentum (the spectroscopic notation P for $L = 1$), and the isospin I and total spin J in the notation $L_{2I,2J}$. In current terminology this is the $\Delta(1232)$ resonance.[2] Since the total width for this state is of order 100 MeV then from the Heisenberg uncertainty principle which can be written as $\Delta E \Delta t \geq \hbar$, we can infer that the lifetime of the $\Delta(1232)$ is of order 10^{-23} seconds.

For such short-lived states the production and decay vertices could never be separated, regardless of the particle's velocity. As scattering energies increased, and as nuclear targets were bombarded with different probes, more and more peaks appeared in cross sections. Determining the properties of these *resonances* became a major area of research beginning about 1951, and spectroscopic studies of resonance production have continued ever since. Information about these resonances, and comparative ratings of the reliability of claimed resonant states, are compiled in the biennial report of the Particle Data Group.[2]
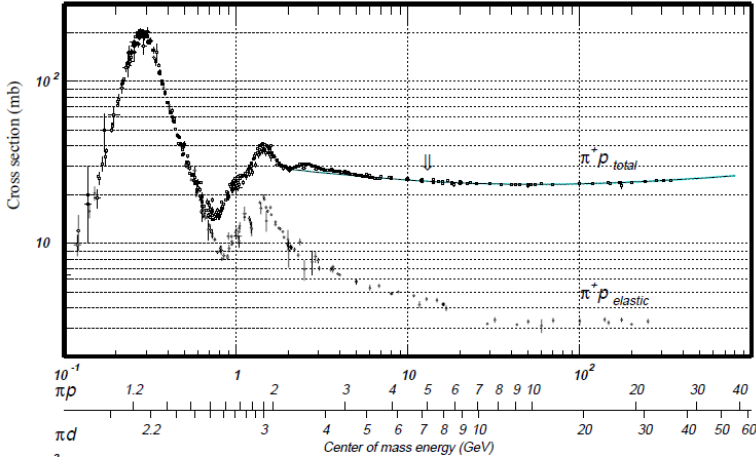
Fig. 2. Total and elastic X-sections for $\pi^+ - p$ scattering, as a function of the laboratory beam momentum in GeV/c (note logarithmic scale), also the CM energy in GeV.

2.1. *Resonances and scattering amplitudes*

Here is an elementary review of bound states and scattering resonances.[3] Consider a two-body scattering process; for simplicity we will initially assume spinless non-relativistic particles in an S-wave state, interacting via a potential $V(r)$. For the time being we will consider two-body scattering in only the elastic channel. The radial wave function can be written as $R(r) = \psi(r)/r$, and the radial Schrödinger equation satisfied by $\psi(r)$ for a given value of the relative momentum k is

$$-\frac{d^2 r\psi_k(r)}{dr^2} + U(r)\psi_k(r) = k^2\psi_k(r) \tag{1}$$

In Eq. (1), $U(r) = 2mV(r)$, m is the reduced mass of the two-body pair, and we adopt units where $\hbar = 1$.

Strong interaction potentials are short-ranged, so we expect $U(r) \to 0$ as $r \to \infty$. In this case at large r we can write

$$\lim_{r\to\infty} \ \psi_k(r) = a(k)e^{-ikr} + b(k)e^{ikr} \tag{2}$$

We can consider the wavefunction ψ to be an analytic function of k. A sufficiently strong attractive potential may support one or more bound states. These are confined states that decay exponentially. They will occur as discrete solutions of the Schrödinger equation of Eq. (1) corresponding to imaginary momentum $k = ik_B$. For this particular value of the momentum, the coefficient $a(ik_B)$ in Eq. (2) must vanish; in this case the wavefunction will decay exponentially at large distances, *i.e.* $\psi_{k_B}(r) \sim e^{-k_B r}$.

The properties of bound states and resonances are related to the behavior of the scattering amplitude in the complex k plane, or equivalently the complex E plane.

The non-relativistic relation between energy and momentum is

$$E = k^2/(2m) + E_{th} \tag{3}$$

From Eq. (3) it is clear that as the phase of the complex variable k varies from $0 \to 2\pi$, the phase of E will change from $0 \to 4\pi$. Thus one sheet of the complex k plane will map onto two sheets of the complex E plane. For the time being consider only the elastic channel (inelastic channels will produce additional sheets of the complex E plane).

A bound state corresponds to a pole of the scattering amplitude $\mathcal{T}(E)$ in the complex k plane at positive imaginary value ik_B. From Eq. (3), bound state poles will appear on the real E axis, below the continuum threshold E_{th}. The upper sheet of the complex E plane is called the physical sheet (the shaded sheet on the left in Fig. 3), and the lower sheet is an unphysical sheet. The two sheets are joined by a cut running along the positive real E axis, beginning at continuum threshold.

If one crosses the cut starting from above, moving from the physical sheet onto the unphysical sheet, the $\mathcal{T}$ matrix is continuous. However, $\mathcal{T}$ is discontinuous if one crosses the cut beginning and remaining on the physical sheet. The discontinuity of the $\mathcal{T}$ matrix across the cut plays an important role in constructing dispersion relations for the scattering amplitude.[3]

Imagine that one has an attractive potential strong enough to produce a bound state. As one decreases the strength of the attractive potential, at some point it will no longer support a bound state. The bound state pole may move onto the second sheet of the complex E plane and become a resonance. A resonance generally produces a peak in the scattering cross section at some energy above elastic thresh-
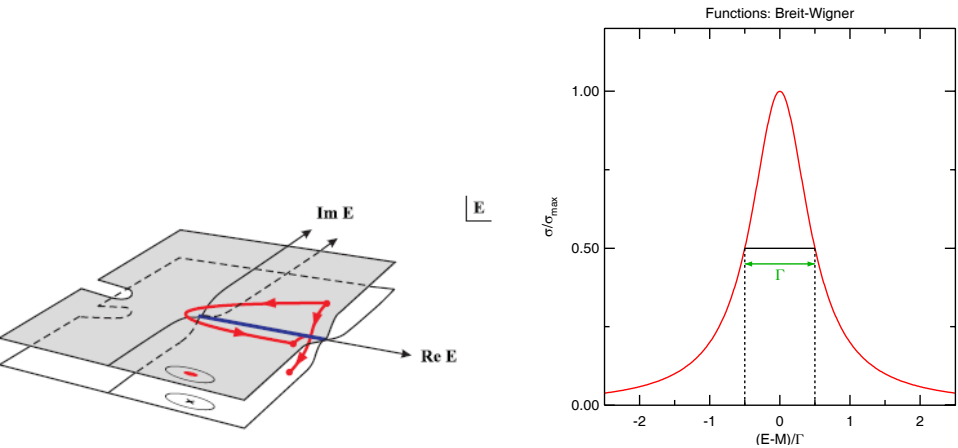

Fig. 3. Left: the complex E plane, the physical sheet (top,shaded) and an unphysical sheet (bottom). A cut runs along the real E axis, beginning at continuum threshold. A resonance is shown as an 'X' on the unphysical sheet. Right: X-section vs. energy for a Breit-Wigner resonance, whose amplitude is given by Eq. (4).

old. The prototypical non-relativistic resonance amplitude was posited by Breit and Wigner,[4] who wrote the scattering amplitude in the vicinity of the resonance in the form

$$\mathcal{T}(E) = g(E)[E - M + i\Gamma/2]^{-1} \tag{4}$$

This leads to a peak in the cross section vs. energy for $E \sim M$, a so-called 'Breit-Wigner' resonance. The right-hand side of Fig. 3 plots the qualitative features of the resulting cross section, which is proportional to the absolute square of the scattering amplitude.

Eq. (4) shows that the resulting cross section will have a peak at energy $E = M$; furthermore, if the quantity $g(E)$ is relatively constant in the vicinity of the peak, then the full width at half maximum around the peak will be given by the quantity Γ. So the location and width of the resonance peak are characterized by the two quantities M and Γ. Eq. (4) shows that the scattering amplitude will have a pole in the complex plane at $E = M - i\Gamma/2$. The resonance pole lies on the unphysical sheet of the complex E plane, below the real E axis, as indicated on the left in Fig. 3.

We can also examine the properties of resonances by defining the scattering or $\mathcal{S}$-matrix.[3] The $\mathcal{T}$ matrix is defined as the amplitude of an outgoing wave solution, corresponding to a unit incoming wave. If we restrict ourself to the elastic channel, the relation between the $\mathcal{S}$ and $\mathcal{T}$ matrix is

$$\mathcal{T}(E) = \frac{S(E) - 1}{2i}; \quad S(E) = e^{2i\delta(E)}; \quad \mathcal{T}(E) = e^{i\delta(E)}\sin(\delta(E)) \tag{5}$$

Unitarity requires that the S-matrix have absolute value one. An attractive (repulsive) potential tends to produce positive (negative) phase shifts. In a one-channel situation with a Breit-Wigner resonance, Eq. (4) shows that $\mathcal{T}(E)$ will be purely imaginary at the resonance position $E = M$. By inspection of Eq. (5), a purely imaginary $\mathcal{T}$-matrix corresponds to $\delta(E = M) = \pi/2$. The location of an elastic resonance (with no background) is characterized by a phase shift of $90°$.

An Argand diagram represents a convenient graphical way to study the behavior of the scattering amplitude, through a two-dimensional plot of the $\mathcal{T}$ matrix vs. energy. The horizontal axis is the real part of the $\mathcal{T}$ matrix and the vertical axis is the imaginary part. For purely elastic scattering the $\mathcal{T}$ matrix moves on a circle (the unitary circle) of radius $1/2$ centered at the point $(0, 1/2)$. The origin of the Argand diagram corresponds to $\delta = 0$. The angle subtended by any point on the unitary circle (relative to the origin) is 2δ. This is illustrated in Fig. 4, which shows an Argand diagram for $\pi - \eta$ scattering.[5] For sufficiently low energies, only the elastic channel is open, and the $\mathcal{T}$ matrix moves on the unitary circle. The phase shift $\delta = \pi/2$ at the position of the $a_0(980)$ resonance. The smaller the width Γ, the faster the phase shift will move through the resonance.

At higher energies, inelastic channels open up. The complex E plane must be expanded to include inelastic channels. Every time an inelastic channel opens, a new cut appears on the real E axis at the inelastic channel threshold, and new
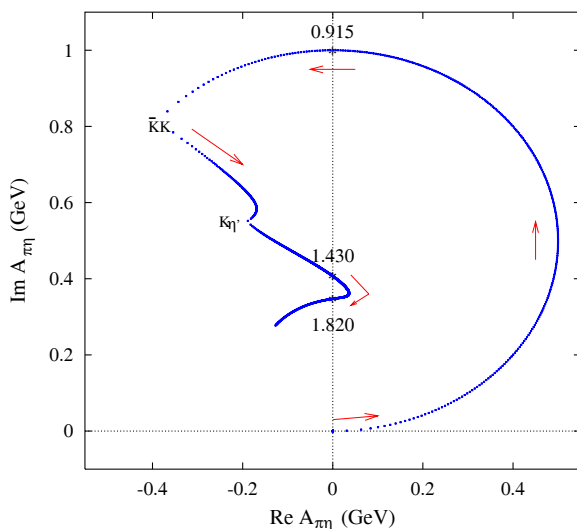
Fig. 4. Argand diagram. At low energies the $\mathcal{T}$ matrix moves on the unitary circle. The phase $\delta = \pi/2$ at an elastic resonance. When inelastic channels open, the $\mathcal{T}$ matrix moves inside the unitary circle.

unphysical sheets appear. Locating a scattering resonance becomes more difficult, as one must determine both the resonance position and the sheet on which it occurs. In the presence of inelastic channels the scattering amplitude becomes a matrix. The quantity $\mathcal{T}_{fi}(E)$ is defined as the coefficient of an outgoing wave in channel f corresponding to unit incoming wave in channel i. Unitarity requires that in the presence of inelastic channels, the elastic $\mathcal{T}$ matrix element must lie inside the unitary circle, and Fig. 4 demonstrates this. Finding resonances in multichannel reactions is likely to rely on sophisticated fitting of scattering amplitudes, or on models that allow one to analytically continue the $\mathcal{T}$ matrix in the complex E plane.

We should emphasize that the simple Breit-Wigner resonance is almost never observed in actual experiments. The $\pi - \pi$ resonance $\rho(770)$ is one of the few examples where this simple resonance picture is valid.[2] In most other cases the situation is far more complex. The goal in analyzing resonant reactions is to identify the location of the pole in the complex energy plane, as this pole is the fundamental dynamical quantity.

2.2. *Identification of resonances with the Dalitz plot*

In the 1950s the catalog of resonances grew at first modestly, then exploded. From a few resonances, one rapidly accumulated a dozen, then eventually greater than one hundred resonant states! A major contributor to this 'zoo' of resonant states lay in the ability for accelerators to produce secondary beams of pions and kaons.

These could be scattered from protons and nuclei, and the final states could be analyzed.

Our simple analysis of resonances was carried out for spinless particles. For particles with spin it is necessary to combine spin and orbital angular momentum in order to determine the total spin and parity of a given resonance. Sophisticated multi-channel partial-wave analyses were developed to extract the scattering amplitudes from experimental reaction data. As energies increased many final states involved three or more strongly interacting particles. A major advance in resonance phenomenology was the introduction of the *Dalitz plot*, a method to analyze three-body (and higher) final states from scattering reactions.[6]

To understand the Dalitz plot, consider a reaction $a + b \to 1 + 2 + 3$ leading to three final-state particles. For the Dalitz plot one graphs the data vs. the squared invariant mass of one pair of final-state particles on one axis and the invariant mass of a second pair on a perpendicular axis. The data points fall inside well defined kinematic limits, since one can show $m_{12}^2 + m_{13}^2 + m_{23}^2 = $ const. Each observed event corresponds to a point inside the Dalitz plot. If the scattering state decays uniformly into three particles, the resulting points will be uniformly distributed. However, two-body resonances appear as enhancements in the Dalitz plot, at the location of the resonant mass. Furthermore, the structure of these bands depends on the spin and parity of the resonant state(s).

Fig. 5 shows the Dalitz plot for the reaction $p + \bar{p} \to 3\pi^0$, from the Crystal Barrel experiment.[7] The data points are represented by shading, with blue denoting few and red signifying many events. The axes are chosen as the invariant mass of two different π^0 pairs. The pion Bose symmetry requires that the Dalitz plot be
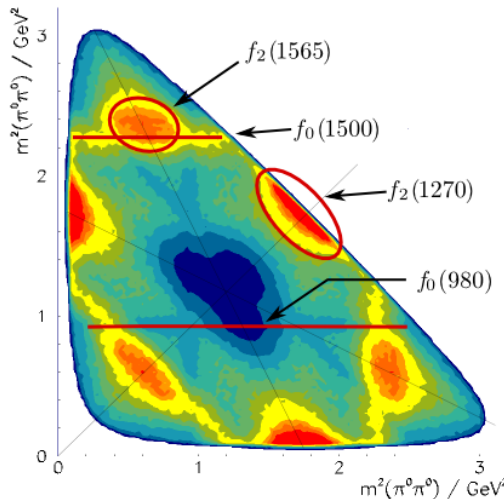

Fig. 5. Dalitz plot for the reaction $p + \bar{p} \to 3\pi^0$. The shading represents the frequency of events, with blue denoting few and red signifying many events. Four resonances are visible in this plot.

symmetric about any axis that exchanges two pions. Four resonances are identified in this plot. The spin-0 $f_0(1500)$ appears as a simple enhancement. Two spin-2 resonances, the $f_2(1270)$ and $f_2(1565)$, have a more complicated shape. The final resonance, the $f_0(980)$ with spin 0, also appears on the plot. Because of quantum mechanical interference between amplitudes, the $f_0(980)$ appears as a *dip* rather than a peak in the distribution of events. The Dalitz plot has proved incredibly useful in enabling experimentalists to locate resonances in reactions with multi-particle final states. In addition, this technique provides a quick estimate of the spin and parity of the observed state.

3. The Quark Structure of Hadrons

By the beginning of the 1960s, there were of order 100 known resonances. These could be classified into *baryon resonances*, strongly interacting states with half-integral total angular momentum J, and *meson resonances*, states with integral (or zero) spin. What had initially been exciting discoveries of a few new states had become almost an embarrassment. This apparent over-abundance of resonances was for awhile quite perplexing. The situation seemed to cry out for introduction of a classification scheme that would make sense of the masses and spins of the plethora of observed resonances.

The first significant breakthrough came in 1960-61, when Ne'eman and Gell-Mann independently showed that nearly all mesons and baryons could be grouped in multiplets defined by the symmetry $SU(3)$.[8] In this scheme, dubbed the 'Eightfold Way' by Gell-Mann, the observed resonances occurred in families when plotted vs. their electric charge, isotopic spin and strangeness values. The graph at left in Fig. 6 shows the $SU(3)$ classification picture for the baryon octet (a multiplet of spin-parity $J^P = 1/2^+$ particles) and decuplet with $J^P = 3/2^+$. The right-hand figure shows the extension of octet and decuplet multiplets when one includes charm quarks.[2]

The baryon octet consists of a pair of particles (the neutron and proton) with zero strangeness, four particles with $S = -1$ consisting of an isotropic triplet (the Σs) and an isosinglet Λ, and a doublet of Ξ with strangeness $S = -2$. One could derive formulae relating the masses of particles within a multiplet; these formulae were generally accurate to within a few percent. Significant support for this classification scheme came in 1962 with the discovery of the Ξ^* doublet with strangeness -2.[9] This left only one 'missing' member of the baryon decuplet, and Gell-Mann predicted a new baryon with spin-parity $3/2^+$ and strangeness -3[8] dubbed the Ω^-; multiplet mass formulae predicted a mass 1680 MeV. In 1964 the Ω^- was discovered at Brookhaven in bubble chamber photographs of $K^- + p$ reactions;[10] its mass was estimated as 1686 MeV.

Similar $SU(3)$ multiplets, with corresponding mass formulae for the multiplet members, could be constructed for the known pseudoscalar and vector mesons. The next step was to find an underlying theory that explained why mesons and baryons
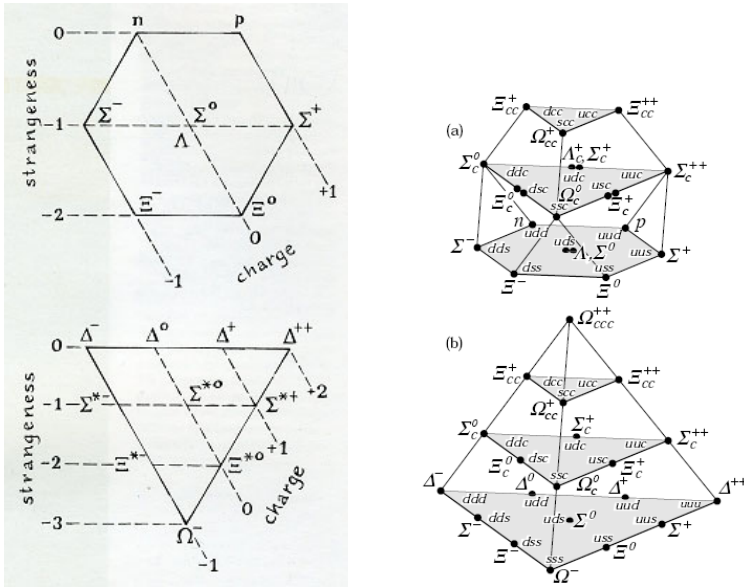
Fig. 6. Left: the baryon octet and decuplet as described by $SU(3)$ symmetry. The vertical axis is strangeness, the horizontal axis is the third component of isotopic spin, and lines of constant electric charge are indicated. Right: extensions of the octet and decuplet including charm quarks.

should inhabit such multiplets. This answer was provided in 1964 independently by Gell-Mann[11] and Zweig,[12] who proposed that baryon and meson structure could be explained naturally by the existence of *quarks* (Zweig called them *aces*). The idea was that there existed three types of quarks, now called *flavors* (up, down and strange), each with its corresponding antiquark. Baryons were composed of three quarks and a meson was a quark-antiquark pair. Individual quarks were fermions with intrinsic spin 1/2; strangeness was an additive property, with the up and down quarks having $S = 0$ and the strange quark $S = -1$. However, in order to produce the observed spectrum of particles, it was necessary that quarks possess electric charges that were a fraction of the proton's charge, specifically the up quark had charge $+2e_p/3$ and the down and strange quarks had charge $-e_p/3$ (an antiquark had opposite strangeness, charge and intrinsic parity from its respective quark).

3.1. *Simple quark models of Hadron structure*

Following the introduction of quarks, the proton was considered to be a three-quark combination consisting of two up quarks and one down quark. This would produce the requisite electric charge of +1 and strangeness zero. In a similar vein, the K^+ meson with strangeness $S = +1$ and charge +1 could be composed of an up quark and a strange antiquark. Furthermore, the spin and parity of a baryon or meson could in principle be constructed by forming various spin-parity combinations of the requisite quarks.

Several groups began to consider what are now known as *constituent quark models* to investigate the apparent properties of these quark combinations, in terms of the known spins, parities and masses of known states.[13] Beginning in the mid 1960s, such efforts had some notable successes. Many of the properties of the baryon octet and decuplet could be reproduced in a constituent quark model with up and down quarks of roughly 340 MeV mass and a strange quark mass in the vicinity of 450 MeV. The three valence quarks in the proton would occupy the lowest states in a confining potential such as an harmonic oscillator. The up quark spins were parallel to the direction of the proton's spin, and the down quark was anti-parallel, with the three quarks coupled to overall spin 1/2 and isospin 1/2. The $\Delta^{++}(1232)$ state was composed of three up quarks, in the same confining potential. Here the quark spins are aligned, producing overall spin-parity $3/2^+$. The strength of the color magnetic interaction could be inferred from the $N - \Delta$ mass splitting. The Λ is composed of *uds* valence quarks. The $N - \Lambda$ splitting gives the mass of the strange constituent quark. In this model of the Λ, the light quarks are coupled to spin 0 and the spin of the strange quark is parallel to the Λ spin direction. In a similar vein, the lowest nonets of pseudoscalar and vector mesons are made by coupling $q\bar{q}$ pairs.

Despite their apparent success in describing the lightest hadron multiplets, constituent quark models encountered a series of problems. Some of these were: (1) The constituent quark model predicts that the first excited baryons should have negative parity. However, the lowest-lying nucleon excited state, the $N(1440)$, has positive parity.[2,13] Furthermore, the masses, spins and parities of excited baryonic and mesonic levels disagreed with constituent quark predictions. (2) Constituent quark masses consistent with the lowest baryon and meson multiplets dramatically over-predicted the pion mass of about 140 MeV. (3) The constituent quark model suggested that quarks in a nucleon were rather lightly bound and non-relativistic. Arguing from experience with atomic nuclei, the constituent quark model suggested that it should be reasonably easy to eject an individual quark from a proton and observe it in a detector. (4) This suggested that fractional charges could be emitted from nucleons. Many extremely sensitive experiments were mounted to search for fractional charges; apart from one or two anomalous results, no isolated fractional charges were ever detected.[14] (5) Constituent quark models required the quarks to be totally symmetric upon interchange of space, spin and isospin quantum numbers. Constituent quark (fermion) wave functions thus violated the Pauli principle.

3.2. *Development of quantum chromodynamics*

The non-observation of free quarks and violation of the Pauli principle led some to postulate that quarks might not be real but might simply represent a mathematical 'mnemonic' device enabling one to predict meson and baryon properties. However, several arguments against the 'reality' of quarks were soon overcome. First was the discovery of the property of *color*, an additive property of quarks which takes

on three values.[15] All stable particles exist only in combinations of quarks and antiquarks that couple to zero net color. For baryons, the resulting three-quark wavefunction is completely color-antisymmetric. Thus quark wavefunctions obey the Pauli principle when one includes color degrees of freedom.

The next significant evidence for quarks came from deep inelastic scattering (DIS) reactions.[16] These involved scattering of leptons (charged leptons, or neutrino-induced charge-changing reactions) from nucleons at very large momentum transfers; one observed only the outgoing lepton and no information regarding the struck nucleon(s). Such reactions showed distinctive features consistent with scattering from elementary pointlike objects inside the proton and neutron. Later in these lectures, we will discuss in considerable detail the history of DIS reactions, what they reveal about baryon structure, and our current understanding of quark-parton distributions in the nucleon.

The quark model was extended with the discovery of three additional quark flavors. In 1974 the charm quark was discovered, with mass roughly 1500 MeV.[17] In 1977 the bottom quark was discovered, with a mass about 4500 MeV.[18] Finally 1995 marked the discovery of the top quark, with a mass roughly 171,000 MeV.[19] The quarks can be grouped into three doublets (u,d) (c,s) and (t,b); in each pair the first quark has charge $+2/3$ and the second quark $-1/3$. Except for the light quarks, the doublets are also characterized by exceptionally large mass splittings.

With the discovery of heavier quark flavors one expects to see additional multiplets of particles containing the heavy quarks (the right side of Fig. 6 shows low-lying multiplets with 4 flavors). We now know that the up and down quark masses are much smaller than the 'constituent' quarks (*u* and *d* 'current quark' masses are roughly 4 MeV and 9 MeV, respectively). Thus, the nucleon mass contains very large contributions from sea quarks and gluons, and there is no way that a non-relativistic perturbative treatment can explain the properties of baryons containing only light quarks. On the other hand, charm and bottom quarks are sufficiently massive that simple models should accurately describe hadrons containing these quarks. Heavy quark effective theory (HQET) has made great use of the simplifications that arise due to the very large mass of the heavy quarks.[20]

We have now a detailed theory of quark interactions. This has culminated in a non-Abelian gauge theory of quarks interacting through the exchange of colored gluons, the carriers of the strong force between quarks. This theory is known as *quantum chromodynamics* or QCD.[21] A first breakthrough was an understanding of the phenomenon of *asymptotic freedom.* Through the Nobel Prize-winning work of Gross and Wilczek and Politzer,[22] it was demonstrated that QCD had the property that at high energies (or alternatively, at very short distances) the interaction between quarks became progressively weaker and weaker. At these very high energies, one could approximate interactions with quarks in terms of free quark interactions. Asymptotic freedom demonstrated why deeply inelastic scattering at very high momentum transfers looks like scattering from free constituents.
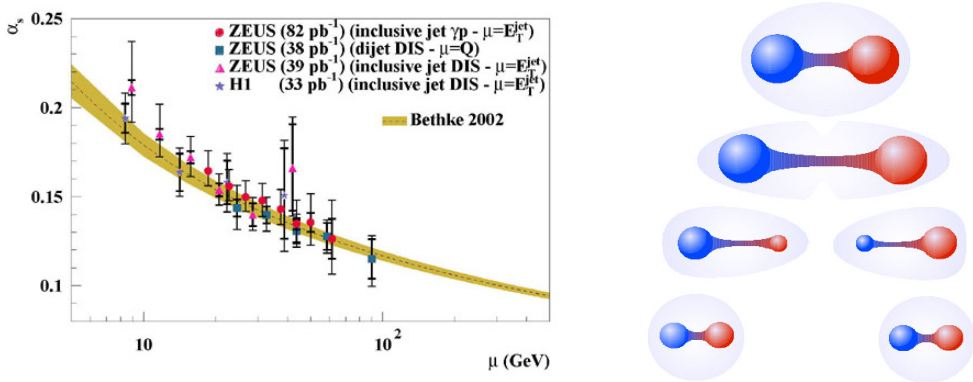
Fig. 7. Left: the value of the QCD strong coupling constant $\alpha_s(E)$ vs. the energy E in GeV. The decrease of the coupling constant with energy demonstrates the phenomenon of asymptotic freedom. Right: schematic picture of quark confinement. As quarks are separated, a 'string' or flux tube forms. When the string is broken a new $q - \bar{q}$ pair is formed.

The left-hand graph in Fig. 7 shows the strong coupling constant α_s as a function of energy. The property of asymptotic freedom is demonstrated by the monotonic decrease in α_s with increasing energy. Conversely, the strong coupling strength increases rapidly at low energies. This means that an understanding of QCD at low energies must deal with very strongly-interacting systems. This is additionally complicated by the realization that gluons have strong self-coupling, unlike the situation in QED. QCD offered formidable challenges to the development of models of strongly interacting systems.

A second major feature of QCD is that an individual colored quark experiences a force that grows monotonically at large distances. This is shown schematically in the right-hand picture in Fig. 7. As a quark-antiquark pair is separated a string or flux tube forms. If one attempts to break the string confining an individual quark, eventually one will produce an additional $q - \bar{q}$ pair (a meson), rather than liberating the quark. Confinement has never been proved analytically in QCD, however it provides a natural explanation for the experimental failure to observe individual quarks. Confinement also occurs in lattice gauge QCD.

The QCD Lagrangian has the form

$$\mathcal{L}_{QCD} = \overline{q}\left(i\gamma^{\mu}\mathcal{D}_{\mu} - m\right)q - \frac{1}{4}G^{a}_{\mu\nu}G^{\mu\nu}_{a}$$
$$G^{a}_{\mu\nu} = \partial_{\mu}G^{a}_{\nu} - \partial_{\nu}G^{a}_{\mu} - gf_{abc}G^{b}_{\mu}G^{c}_{\nu} \tag{6}$$

In Eq. (6) one sums over all flavors of quark fields, represented by q, the quantities G^{a}_{μ} represent the eight gluon fields, and the term $G^{a}_{\mu\nu}$ is the QCD analog of the electromagnetic tensor $F^{\mu\nu}$ which occurs in quantum electrodynamics. An excellent summary of QCD is given in the Handbook of Perturbative QCD.[23]

As we have mentioned, the problem of solving the QCD Lagrangian at low energies turned out to be formidable. Our best estimate of u and d quark mass is less than 10 MeV, which leads to the astonishing conclusion that the 'current quark' masses make up only about 2% of the proton mass! The remainder of the mass must consist of very large contributions from gluons and the sea. At present, the only viable means to solve QCD at low energies appears to be *lattice gauge* techniques. In this case one discretizes space-time on a lattice. Good numerical results can be achieved by rotating to Euclidean (imaginary) time. The continuum limit is achieved as the lattice spacing $a \to 0$. One discretizes the Yang-Mills action for the QCD Lagrangian, defines the quark fields on the lattice sites, and uses Monte Carlo techniques for solving the resulting multi-dimensional integrals. Lectures on lattice gauge theory will be given at this workshop by N. Mathur.

4. DIS and the Partonic Structure of Baryons

Our current view is that hadrons are composed of structureless elementary particles, quarks and antiquarks, whose strong interactions are mediated by exchange of colored gluons. We now review the history of the experimental data that demonstrated the quark nature of baryon structure, and indicates that quarks have no internal structure. The first significant evidence for the elementary nature of quarks came from deep inelastic scattering (DIS) reactions.[16] These involved scattering of leptons (initially charged leptons, or neutrino-induced charge-changing reactions) from nucleons at very large momentum transfers. In these reactions one observed only the outgoing charged lepton and no information regarding the struck nucleon(s). Such reactions carried out initially with electron beams at the Stanford Linear Accelerator Center (SLAC) and with neutrinos at CERN, showed distinctive features consistent with scattering from elementary pointlike objects inside the proton and neutron. Initially these constituents were called 'partons' but these were later shown to be quarks and antiquarks.[13]

Consider DIS reactions induced by scattering of charged leptons from a nucleon, mediated by exchange of a virtual photon, as shown schematically in Fig. 8. We can describe the process in terms of two relativistic invariants, which we will define as Q^2 and x, defined as $Q^2 = -q^2$ and $x = Q^2/(2M\nu)$; here the 4-momentum transfer Q^2 is large, and $\nu = E - E'$ is the lepton energy loss.

The cross section for DIS with a charged lepton can be written as the contraction of a lepton tensor $L^{\mu\nu}$ and a hadron tensor $W_{\mu\nu}$, where

$$\frac{d^2\sigma}{dxdy} = \frac{2\pi\alpha^2}{Q^4} L^{\mu\nu} W_{\mu\nu}$$

$$W_{\mu\nu} = \left(-g_{\mu\nu} + \frac{q_\mu q_\nu}{q^2}\right) F_1^\gamma(x, Q^2) + \frac{P_\mu P_\nu}{P \cdot q} F_2^\gamma(x, Q^2) \qquad (7)$$

The cross section for lepton-nucleon DIS (mediated by photon exchange) thus depends upon two structure functions F_1^γ and F_2^γ. Each structure function depends

on the invariants x and Q^2. In a frame of reference where the proton is moving with infinite speed, the quantity x gives the fraction of the nucleon's momentum carried by the struck parton. In Fig. 8, one could also exchange a weak vector boson Z_0 between the charged lepton and nucleon. This would give rise to a third structure function denoted F_3, which would be associated with parity-violating transitions.

Over the past thirty years, many experiments have been devoted to measuring these structure functions. The left-hand side of Fig. 9 shows measurements of the structure function F_2^γ. Values of F_2^γ are plotted for various values of x, vs. Q^2. The curves for different x values are offset so that they do not lie on top of one another. The values have been obtained from a series of different experiments.[24] There are electron-induced experiments from the SLAC linear collider and the HERA electron-proton collider (its two detectors, H1 and ZEUS), and experiments using high-energy muons from the BCDMS and New Muon Collaboration (NMC) at CERN and experiment E665 from Fermilab.

The first dramatic feature of the resulting structure function is the precision that has been obtained with these F_2 measurements. Except for the very highest values of Q^2 that can be achieved for a given x, the errors are very small indeed. The second striking feature is that, over a Q^2 range of five orders of magnitude, the structure function F_2^γ varies very little. The constancy of the F_2 structure functions was clear evidence that scattering was occurring from elementary pointlike constituents; otherwise the structure function would be governed by a form factor, and over this wide range of Q^2 a form factor should decrease by orders of magnitude. Friedman, Kendall and Taylor shared the 1990 Nobel Prize in physics for their DIS measurements in $e - p$ reactions at SLAC that first demonstrated this 'scaling' behavior in the structure functions.[25]

One can also measure polarized structure functions. For scattering of unpolarized leptons on polarized nucleons, the cross section asymmetry resulting from virtual photon exchange is related to the polarized structure function $g_1(x, Q^2)$, where one has

$$\frac{d^2\sigma(N_\Rightarrow^\rightarrow) - d^2\sigma(N_\Leftarrow^\rightarrow)}{dx\,dy} \sim x g_1(x, Q^2) \tag{8}$$
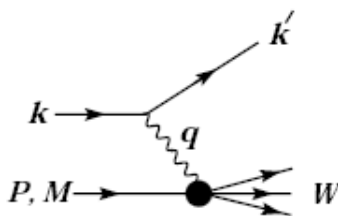

Fig. 8. Schematic diagram of deep inelastic scattering of charged lepton, with initial and final momenta k and k', from a nucleon with momentum P, through exchange of a virtual photon.
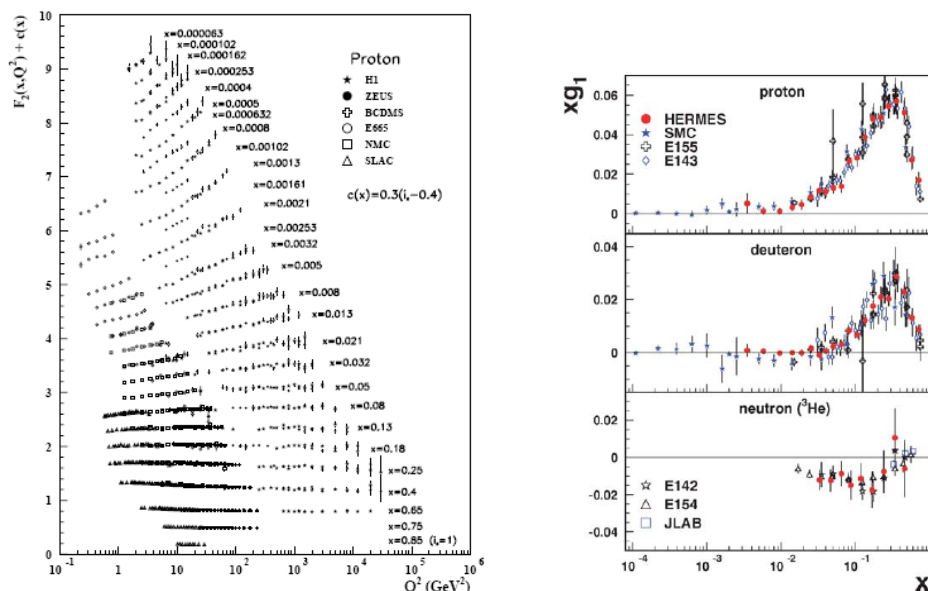
Fig. 9. Left: the structure function F_2^γ obtained from DIS from charged leptons on protons. F_2 is plotted for different values of x as a function of Q^2. Right: polarized structure function $xg_1(x, Q^2)$, obtained for a fixed value $Q^2 = 10$ GeV^2 and plotted for p, D and n.

In Eq. (8), the cross section $\sigma(N_{\Rightarrow}^{\rightarrow})$ is taken for a nucleon whose spin is parallel to the direction of the incident lepton beam, and subtracted from the cross section $\sigma(N_{\Leftarrow}^{\rightarrow})$ where the nucleon's spin is antiparallel. The right-hand side of Fig. 9 plots xg_1 vs. x for experiments with protons, deuteron, and neutron (the neutron result is extracted from experiments on ^{3}He).[26] Here, the experiments are all extrapolated to the same value $Q^2 = 10$ GeV^2. One can also extract additional structure functions when the nucleon spin is transverse to the plane of the four-momentum transfer.

4.1. *A Qualitative picture of proton structure*

In Sec. 3.1, we presented a naive picture of the structure of the proton, based on the constituent quark model. Based on our current understanding of QCD dynamics, and our knowledge that the 'bare' masses of u and d quarks are extremely small, we need to modify this simplistic picture. We know that at low energies quarks are coupled to gluons with a coupling constant. Furthermore, gluons exhibit self-coupling and are also coupled to quark-antiquark pairs. These couplings are shown schematically in the left-hand figure in Fig. 10.

Imagine that we start with a nucleon containing just three 'valence' quarks. Through the QCD couplings shown in the left-hand side of Fig. 10, the valence quarks can radiate gluons, which in turn can produce more gluons and quark-antiquark pairs. Starting with a proton that contains only 'valence' quarks, QCD
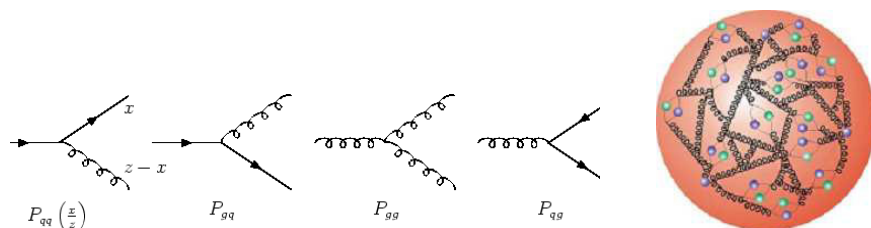
Fig. 10. Left: schematic picture of quark and gluon couplings. A quark can radiate a gluon; gluons exhibit self-coupling; and a gluon can radiate a quark-antiquark pair. Right: a cartoon showing a 'valence plus sea and glue' picture of the proton.

radiation can produce a proton containing a 'sea' of gluons and quark-antiquark pairs, as depicted by the cartoon on the right in Fig. 10.

We have presented two naive pictures of the proton, one with just three constituent quarks and the second with many additional sea quarks and gluons. What we expect in a given DIS reaction will depend upon the value of x. Note that from the left-hand side of Fig. 10, quark or gluon radiation involves sharing parton momentum with the additional constituents. As QCD radiation produces more and more partons, each parton will carry less of the proton momentum and will correspond to partons with progressively smaller values of x. Consequently, the quantity x which denotes the fraction of the proton's momentum carried by the struck quark, will determine which picture of the nucleon will be 'seen' in that reaction. At large values of x the nucleon will look like three 'valence' quarks; as x decreases we expect a 'sea' of quark-antiquark pairs and gluons.

A crucial ingredient is the probability of finding partons that carry a given fraction x of the proton's momentum. Quantities that satisfy this definition are called **P**arton **D**istribution **F**unctions, or PDFs. Define the quantity $q(x)$, $q = u, \bar{u}, d, \bar{d}, \ldots$. For a proton with very high momentum, $q(x)$ is the probability that a quark of that flavor carries a momentum fraction between x and $x + dx$; similarly a gluon PDF $g(x)$ gives the probability that a gluon carries momentum fraction x. We should also include a dependence upon Q^2, as we will later show that PDFs have a slow (logarithmic) dependence on Q^2.

From Fig. 10, antiquarks in the proton will arise mainly from gluon radiation of $q - \bar{q}$ pairs. Thus we expect all antiquarks to be part of the nucleon 'sea' that is radiated by gluons. Light (u and d) quarks have two sources: one component of these PDFs is part of the 'valence' distribution; a second component arises from gluon radiation. Now q and $\bar{q}$ arising from gluon radiation have equal probability. For a given quark flavor we thus define valence quark distributions $q_v(x) = q(x) - \bar{q}(x)$. If all antiquark distributions arise from gluon radiation, then subtracting the antiquark PDF from the quark PDF cancels out the 'sea' quark contribution leaving just the 'valence' part.

4.2. *Relation between DIS and quark PDFs*

In a preceding section we showed that DIS reactions could be described in terms of a small number of structure functions. An obvious question is: what is the relation between the structure functions and the quark PDFs that we have just defined? To lowest order in QCD, structure functions have very simple relations in terms of PDFs. For example, the unpolarized and polarized structure functions F_2^γ and g_1^γ that occur in DIS from charged leptons (arising from virtual photon exchange between electron and proton as shown in Fig. 8) have the form

$$F_2^\gamma(x, Q^2) = x \sum_j e_j^2 \left[q_j(x) + \bar{q}_j(x)\right] = x \left[\frac{4(u + \bar{u}) + d + \bar{d} + s + \bar{s}}{9}\right]$$

$$g_1^\gamma(x, Q^2) = \sum_j \frac{e_j^2}{2} \left[\Delta q_j(x) + \Delta \bar{q}_j(x)\right]$$

$$= \frac{4(\Delta u + \Delta \bar{u}) + \Delta d + \Delta \bar{d} + \Delta s + \Delta \bar{s}}{18} \ . \tag{9}$$

In Eq. (9), e_j is the charge of a quark with flavor q_j, and $\Delta q(x) = \overrightarrow{q}(x) - \overleftarrow{q}(x)$, where $\overrightarrow{q}(x)$ ($\overleftarrow{q}(x)$) is the probability for finding a quark whose spin is parallel (antiparallel) to the proton spin. Eq. (9) includes contributions from three flavors.

If we include DIS from charged-current ν leptoproduction, *e.g.* $e^- + p \to \nu + X$, then the reaction is characterized by a virtual W^- being absorbed by the proton. In that case three of the structure functions that appear in this reaction can be written in lowest order QCD as

$$F_2^{W^-}(x, Q^2) = 2x \left[u + \bar{d} + \bar{s}\right]$$

$$xF_3^{W^-}(x, Q^2) = 2x \left[u - \bar{d} - \bar{s}\right]$$

$$g_1^{W^-}(x, Q^2) = \Delta u + \Delta \bar{d} + \Delta \bar{s} \ . \tag{10}$$

The additional structure function $xF_3^{W^-}$ is present because exchange of the weak vector boson W^- contains a piece that violates parity; here the structure function F_3 characterizes the parity-violating part of this interaction. Note in both Eqs. (9) and (10), we have not included the dependence of the PDFs on x and Q^2.

The above equations show that different observables are sensitive to different combinations of PDFs. Thus by carrying out a series experiments employing lepton, neutrino and hadron beams, and including unpolarized measurements with both longitudinal and transversely polarized beams and targets, one can gain differential sensitivity to specific quark and gluon PDFs. By amassing a large body of experimental data from many different experiments one can perform a global analysis of all of the experimental data and extract best values for the quark and gluon PDFs.[2]

We mentioned previously that PDFs at different Q^2 are related by QCD, through what are called the DGLAP evolution equations.[27] These are convolution relations relating the PDFs for a given value of x at different Q^2 values. Thus if one knows the

PDFs at one (sufficiently large) value of Q^2, they can be determined at higher values of Q^2 through these evolution equations. The non-singlet (valence) PDFs satisfy their own integro-differential equation, while the sea quark and gluon distributions are coupled,

$$\frac{\partial q_V}{\partial \ln \mu^2} = \frac{\alpha_s(\mu^2)}{2\pi} P_{qq} \otimes q_V$$

$$\frac{\partial}{\partial \ln \mu^2} \begin{pmatrix} q_s \\ g \end{pmatrix} = \frac{\alpha_s(\mu^2)}{2\pi} \begin{pmatrix} P_{qq} & 2n_f P_{qg} \\ P_{gq} & P_{gg} \end{pmatrix} \otimes \begin{pmatrix} q_s \\ g \end{pmatrix}$$

$$\text{where} \quad P \otimes f \equiv \int_x^1 \frac{dy}{y} P(y) f\left(\frac{x}{y}\right) \tag{11}$$

In Eq. (11), the quantity n_f refers to the number of active quark flavors participating in the reaction, and the evolution kernels P_{ij} can be determined from perturbation theory.[23]

5. Experimentally Determined Parton Distribution Functions

Over the past three decades a very large number of precision experiments have been performed, designed to elucidate the partonic structure of nucleons. The pioneering experiments at SLAC were fixed-target experiments, with a beam of high-energy electrons incident on a fixed target. Such experiments can reach the largest values of x, and are being continued today at Jefferson Laboratory. Another class of experiments involved colliding beams. For example, the HERA accelerator at DESY, which has recently been closed down, was an asymmetric collider where 30 GeV electrons collided with 820 GeV protons. Fig. 9 shows that the two HERA detectors H1 and ZEUS covered an enormous range of x and Q^2, and also reached to the lowest values of x. HERA also had a smaller fixed-target program, HERMES, which studied electron collisions with polarized nucleon targets.

Useful information regarding parton distributions has been obtained from Drell-Yan processes.[28] These processes involve the production of large invariant-mass $\mu^+ - \mu^-$ pairs from nucleon-nucleon and nucleon-nucleus reactions. These processes occur when a q ($\bar{q}$) from the projectile annihilates a $\bar{q}$ (q) of the same flavor from the target, producing a virtual photon that decays to a pair of oppositely charged muons. Such processes are quite sensitive to the $\bar{q}$ PDFs in the proton.

Information on s quark distributions is obtained from neutrino charge-changing reactions. In such processes an incident ν_μ produces a μ^- and a virtual W^+. The W strikes an s quark and produces a c quark. The charm quark subsequently undergoes semi-leptonic decay producing a μ^+. The signature of these reactions is production of oppositely charged high-energy muons from a neutrino beam, and provides the most reliable information on s quark PDFs. Production of $\mu^+ - \mu^-$ pairs from a $\bar{\nu}$ beam is sensitive to $\bar{s}$ PDFs.[29]

Information from a wide array of high-energy experiments is placed in a global fit to parton distribution functions. From these experiments one can extract the struc-
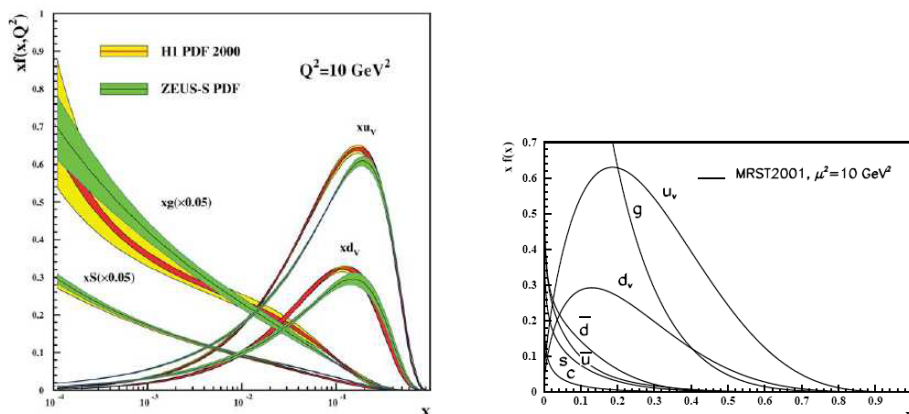
Fig. 11. Proton PDFs. Values of $xq(x)$ determined from global fits to high-energy data evolved to $Q^2 = 10$ GeV^2. Left: width of band gives a measure of the uncertainty in the PDF. Yellow: determined from H1 HERA data; green: determined from ZEUS data. Right: a linear plot in x, separating different sea quark flavors.

ture functions. By now, the relation between the structure functions and PDFs is presented at least to next to leading order (NLO) in QCD. By now quite sophisticated global fitting routines are employed to extract the parton distributions. Two of the best known of these are employed by the CTEQ collaboration,[30] and by the MRST group.[31] The DGLAP evolution equations of Eq. (11) are used to connect parton distributions at different Q^2 values. The resulting PDFs are plotted at one particular value of Q^2; PDFs at different values of Q^2 can be obtained from the evolution equations.

Fig. 11 shows our current knowledge of quark PDFs. Quark and gluon PDFS multiplied by x are plotted vs. x. The left figure is a semi-log plot and the right-hand figure is a linear plot that separates different sea quark flavors. The PDFs are evolved to $Q^2 = 10$ GeV^2. The HERA data is most extensive. There are small differences between the PDFs depending on data from the H1 detector (yellow band) or from ZEUS (green band).[24] The width of the bands gives an indication of the uncertainty in the PDFs. The quantity xS is the sum of all sea quark PDFs.

Our naive picture suggested that at large x, the proton should be composed primarily of valence quarks. This agrees with the analyses; for large x the valence quarks dominate the PDFs. For small x the sea and glue distributions rise rapidly. Note that in the left graph of Fig. 11 the sea and gluon distributions have been divided by 20. Thus the sea and glue grow extremely rapidly at small x.

The valence PDFs obey quark normalization conditions. Their first moments give the total number of valence quarks in the proton, $\langle u_v(x) \rangle = 2$, $\langle d_v(x) \rangle = 1$. where the brackets denote integration over all x. One thus expects that $u_v(x) \sim 2d_v(x)$. Fig. 11 shows that this is approximately the case.

In the right-hand side of Fig. 11 the sea PDFs are separated by flavor. The s quark distribution is roughly half the average of u and d sea quark PDFs. The c quark distribution is much smaller than the other sea quark distributions, due to the much larger c quark mass. The right side of Fig. 11 shows that the $\bar{d}$ distribution is larger than the $\bar{u}$ distribution. We can understand this from 'meson cloud' models of the nucleon.[32] Such models include contributions particularly from the pion cloud. The proton can undergo virtual transitions $p \to n + \pi^+$. The valence quark content of the π^+ is $u - \bar{d}$. Thus one contribution to the $\bar{d}$ distribution arises from scattering from the $\bar{d}$ in the π^+ cloud of the proton. 'Meson cloud' models can account at least qualitatively for the magnitude and x distribution of the $\bar{d} - \bar{u}$ distribution in the proton.

6. Surprising Features of Parton Distribution Functions

In the preceding section we reviewed qualitative features of quark PDFs obtained from global fits to high energy. Now we will focus on some of the surprises that have occurred as we have unraveled the structure of the proton.

6.1. *Momentum carried by the proton*

In our simplest picture with a proton composed of three constituent quarks, each 'constituent' quark should carry roughly $1/3$ of the proton's momentum. The valence quark distributions shown in Fig. 11 peak at lower values of x; u_v peaks at $x \sim 0.2$ and d_v peaks at an even smaller x value. A major surprise occurred with the quantitative understanding of the distribution of the proton's momentum. The total proton momentum can be represented by a sum rule

$$\left\langle \sum_j x(q_j(x) + \bar{q}_j(x)) + xg(x) \right\rangle = 1 \qquad (12)$$

Eq. (12) expresses the fact that the proton momentum can be divided into the total amount carried respectively by quarks, antiquarks and gluons. At high values of Q^2, the total proton momentum carried by valence quarks is roughly 35%, sea quarks carry 15%, and gluons carry 50% of the momentum. This differs dramatically from the naive picture where valence quarks would carry all of the proton's momentum. It is one more indication of the extremely important role of glue, both in constituting the mass of the nucleon and now in terms of the proton linear momentum.

6.2. *Nuclear modification of structure functions*

Another major surprise is the realization that even at very high energies, structure functions in nuclei differ from those in the proton. First let us discuss what we expect for parton distributions in the neutron. The operation of charge symmetry (CS) interchanges p and n; this is a specific rotation in isospin space (a rotation of $180°$ about the '2' axis in isospace) that interchanges p and n labels. At low energies, charge symmetry is obeyed extremely well, with most low-energy amplitudes

obeying CS at the 1% level or better. So, it is 'natural' for CS also to hold at high energies. In principle one can test the validity of parton charge symmetry; no violations have been observed and present upper limits of partonic charge symmetry are at the level of several percent.[33]

If one assumes the validity of charge symmetry at the partonic level, then all PDFs for the neutron can be written in terms of those for the proton. Charge symmetry predicts that $u^n(x) = d^p(x)$ and $d^n(x) = u^p(x)$; it also predicts that s and c PDFs should be identical for n and p. Analogous equations hold for antiquarks. Since heavier nuclei have roughly equal numbers of neutrons and protons, in comparing nuclear structure functions to those in the nucleon it makes sense to compare heavier nuclei with the deuteron.

To date, there have been extensive measurements of the F_2 structure function for DIS of charged leptons from nuclei. One plots the F_2 structure function per nucleon arising from virtual photon exchange, and constructs the ratio of the structure function for a nucleus with A nucleons with that for the deuteron,

$$R_A(x) = F_2^A(x)/F_2^D(x) \tag{13}$$

Fig. 12 plots the quantity $R_A(x)$ vs. x for various nuclei, from Arneodo.[34] The top curve shows the qualitative behavior of $R_A(x)$ vs. x. The bottom points are the results of this ratio for experiments on four nuclei. The diamonds and open circles are results on C and Ca respectively from NMC. The solid squares show results on Al from SLAC. The solid triangles are results on Xe from E665.

The experimental points show rather dramatically that the structure function F_2 have a distinct A dependence. Furthermore, the nuclear effects on the F_2 structure functions can be divided into roughly three distinct regions: a 'shadowing' region for small $x < 0.05$; a 'Fermi smearing' region for very large x; and what is called the 'EMC effect' in the region of x between the shadowing and Fermi smearing regions. Fig. 12 shows dramatically that even at high energies, there remain significant differences between DIS from nuclei and scattering from individual free nucleons.

The A-dependence of $R_A(x)$ for intermediate x is called the 'EMC effect' after the definitive experiments in the early 1980s from the European Muon Collaboration at CERN.[35] These experimental results were extremely surprising. At least in the regime of intermediate x, it was widely assumed that at sufficiently high energies, nuclear DIS would look just like DIS from quarks in individual free nucleons.

Since $x = Q^2/(2M\nu)$, the very large x region corresponds to the largest values of Q^2 for a given incident energy. On a nuclear target, scattering of a virtual photon at large x values will be greatly affected by the nuclear Fermi momentum. For collisions at very large Q^2 to the nucleus, nucleons with Fermi momentum moving towards (away from) the virtual photon will experience collisions at a relatively much larger (smaller) value of Q^2. Since $F_2 \to 0$ rapidly at large x, Fermi smearing effects will produce nuclear F_2 that are much larger than that for a free nucleon. Thus we expect to see a very rapid increase in $R_A(x)$ at sufficiently high x due to these Fermi smearing effects, in agreement with the results shown in Fig. 12.

6.2.1. *Nuclear effects in the shadowing regime*

Fig. 12 shows that in the region of small $x \leq 0.05$, the ratio $R_A(x)$ decreases monotonically with decreasing x, and $R_A(x)$ shows some sign of approaching a constant value at very small x. The experimental points show that this curve is not universal but has a characteristic A dependence, with the 'shadowing' corrections becoming larger with increasing A. For a given incident energy the small x region corresponds to the smallest values of Q^2. Even for very high energies, sufficiently small x values can correspond to the range $1 \leq Q^2 \leq 5\ \mathrm{GeV}^2$. In this region, viewed from the rest frame of the nucleus, we expect to see effects arising from transitions of the virtual photon to vector mesons. From the CVC (Conserved Vector Current) hypothesis, a virtual photon will occasionally make a transition to a vector meson, particularly a $\rho(770)$. Since photons interact weakly with matter we expect the impulse approximation to be valid, in which case $R_A(x)$ should be one. However, the ρ interacts very strongly and at these energies will be strongly absorbed. To
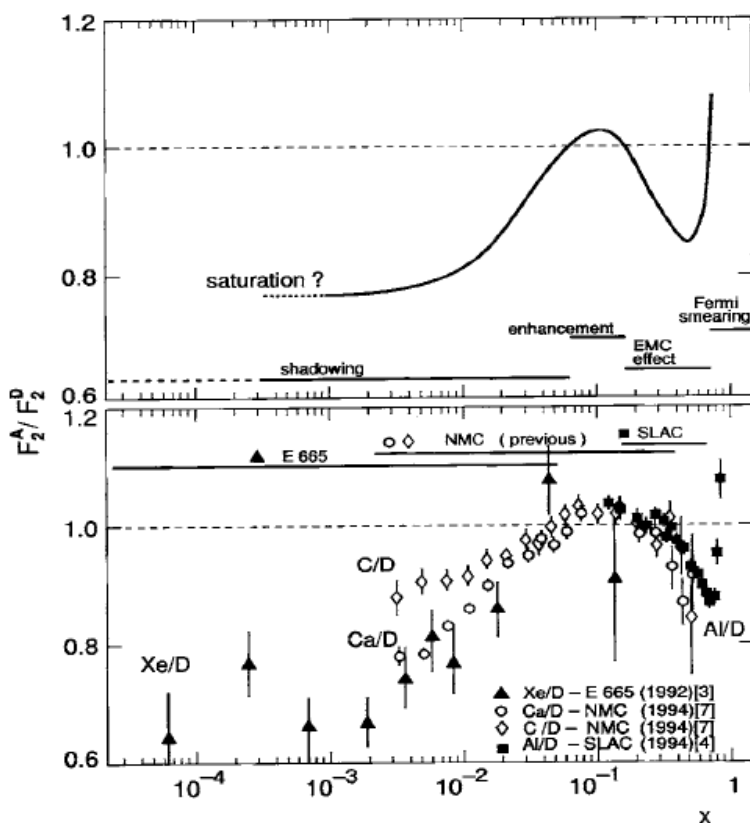

Fig. 12. The ratio of F_2 structure functions for nuclei to those for the deuteron, vs. x. Top: a curve that shows the qualitative behavior of this ratio vs. x. Bottom: results of this ratio for experiments on four nuclei.

a good approximation the cross section for the ρ should vary as the area of the nucleus, $\sigma_\rho \sim R^2 \sim A^{2/3}$. These are called 'shadowing' corrections. As soon as a ρ encounters a nucleon it is absorbed. Nucleons on the 'far' side of the nucleus are 'shadowed' from seeing the ρ by the nucleons on the 'near' side.

The nuclear F_2 structure function per nucleon arising from $\gamma^* \to \rho$ transitions should behave like $A^{2/3}/A \sim A^{-1/3}$. One would expect to see $R_A(x) \sim A^{-1/3}$ if 100% of the nuclear cross section arose from such transitions. Although quantitative calculations are significantly more complicated than this simple picture, the qualitative behavior is correct. First, shadowing corrections decrease F_2^A in heavier nuclei and one expects $R_A(x) < 1$; the shadowing corrections are largest at the smallest values of x; and finally shadowing corrections become larger with increasing A. All of these are observed in the data. If we consider nuclear DIS reactions in the infinite momentum frame, then shadowing should occur through gluon recombination and interference effects. A picture due to Gribov[36] relates shadowing to diffractive effects. This picture relates two different scattering phenomena and leads to interesting predictions but it is not yet clear that it provides quantitative agreement with experiment.

6.2.2. *The 'EMC effect'*

The final nuclear effect involves a slight increase $R_A(x) > 1$ just below $x = 0.1$, followed by a monotonic decrease in the region $0.1 \leq x \leq 0.6$; this is called the 'EMC Effect' from its discovery in the early 1980s by the European Muon Collaboration. Until that time one expected that nuclear DIS in this region would just be the sum of individual lepton-nucleon DIS; thus we would expect $F_2(x)$ per nucleon to be the same regardless of A.

The EMC Effect appears to be nearly universal; the curves of $R_A(x)$ for various nuclei lie almost on top of one another. The EMC Effect inspired more than 1000 papers that considered the origin and explanation of this nuclear effect.[35] Kulagin and Petti[37] claim that three different mechanisms play a role in the EMC Effect. The first two involve nuclear binding and off-shell effects on nuclear structure functions. Treating bound nucleons non-relativistically and using weak-binding approximations, one can write F_2^A as a product of free F_2 structure functions for p and n, convoluted with the virtuality of the bound nucleons. An additional contribution to F_2^A comes from scattering of the virtual photon from the meson cloud, particularly the pion cloud. The left side of Fig. 13 plots the ratio $R_A(x)$ vs. x for gold.[37] The dotted curve includes only Fermi momentum plus nuclear binding (FMB) effects. The dashed curve includes the FMB plus off-shell (OS) effects. The dot-dashed curve adds nuclear pion (PI) effects; and the solid curve is the full result including nuclear shadowing (NS) effects. Shadowing is significant only in the shadowing regime. Nuclear pion effects are significant only for $x \leq 0.2$. In the EMC region the most important processes are claimed to be binding and off-shell effects, although others have argued that nuclear pion effects are dominant.[35]
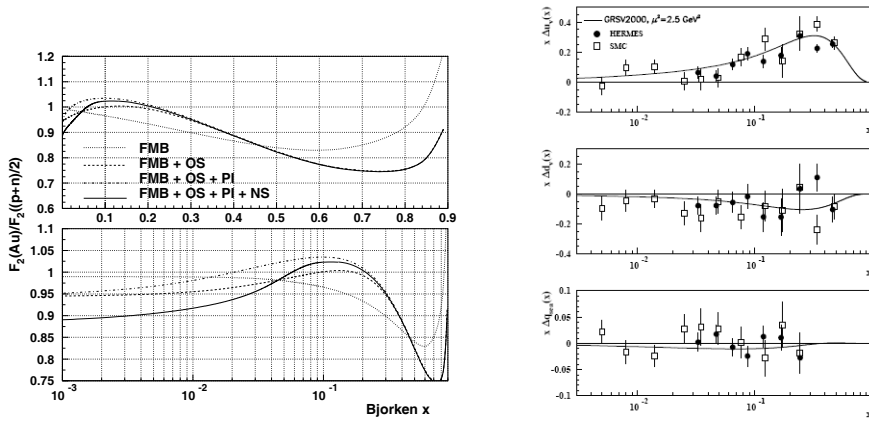
Fig. 13. Left: the ratio $R_A(x)$ from Eq. (13) of F_2 structure functions for gold to those for the deuteron, vs. x. Top: linear plot of $R_A(x)$; bottom: semi-log plot. Right: spin-dependent PDFs. Top: $x\Delta u_V(x)$ vs. x; middle: $x\Delta d_V(x)$; bottom: $x\Delta q_{sea}(x)$. Curves evolved to $Q^2 = 2.5$ GeV^2.

6.3. *Polarized DIS and the spin of the proton*

As was mentioned in Sec. 4.2, one can extract the quark longitudinal spin-dependent PDFs $x\Delta u(x)$ and $x\Delta d(x)$ through measurements using polarized protons. Eq. (8) relates the polarized structure function $g_1(x)$ to the asymmetry in deep inelastic scattering for unpolarized leptons on longitudinally polarized nucleons. Eq. (9) relates the polarized structure function to the spin-dependent PDFs. On the right in Fig. 13 we plot the longitudinal spin-dependent PDFs that have been extracted from experiment.

The experimental results[38] are from the Spin Muon Collaboration (SMC) (open squares) and HERMES (solid circles). HERMES took semi-inclusive DIS measurements from polarized proton or deuteron targets, where one measured a final-state meson (π or K) in coincidence with the scattered lepton. Such semi-inclusive DIS experiments allow one to enhance contributions from particular spin-dependent quark flavors. As can be seen from Fig. 13, one obtains $\Delta u_V(x) > 0$ and $\Delta d_V(x) < 0$, and in magnitude $\Delta u_V(x) > |\Delta d_V(x)|$, in agreement with naive quark model expectation. It is also clear that the sea quark contribution to the nucleon spin is small and consistent with zero for all measured x values.

6.3.1. *The 'proton spin crisis'*

We can write a sum rule for the total spin of the proton,

$$\frac{1}{2} = \frac{1}{2}\Delta\Sigma + \Delta G + L_q + L_g \quad , \tag{14}$$

In Eq. (14), $\Delta\Sigma$ is the total spin carried by quarks and antiquarks, ΔG is the total spin carried by gluons, and the quantities L_q and L_g are respectively the total

orbital angular momentum carried by quarks and gluons. The capital letters refer to the first moment over x, *i.e.*

$$\Delta\Sigma = \left\langle \sum_q \Delta q(x) + \Delta\bar{q}(x) \right\rangle ; \quad \Delta G = \langle \Delta g(x) \rangle \tag{15}$$

In the constituent quark picture the first moments of quark spin PDFs are given by

$$\Delta U = \frac{4}{3}, \ \Delta D = -\frac{1}{3}, \ \Delta S = 0, \ \Delta\Sigma = \Delta U + \Delta D + \Delta S = 1; \tag{16}$$

Eq. (16) shows that in the naive quark picture all the proton spin arises from the quarks, with zero contribution from gluons or orbital angular momentum.

The first quantitative measurements of the quark spin PDFs gave results like $\Delta\Sigma \sim 0.2\pm0.2$. Not only was the total proton spin carried by quarks far smaller than 100%, these results were consistent with *zero* proton spin being carried by quarks! This surprising and puzzling result was termed the 'proton spin crisis.' We have now obtained more precise results and the current best value is $\Delta\Sigma \sim 0.3 \pm 0.05$. So the total proton spin carried by quarks is somewhat larger than it had appeared, and it is no longer consistent with zero. Nevertheless, one very important quantitative question is exactly how do we account for the spin carried by the proton[39]? A related question is whether or not the current experimental result $\Delta\Sigma \sim 0.3$ for the proton spin carried by quarks is surprising.

6.3.2. *Contribution of polarized glue to proton spin*

Previously we saw that gluons carried a surprisingly large fraction of the proton momentum. It seems natural to ask whether gluons might also carry much of the proton spin. In order to answer this important question, dedicated experiments to measure gluon contributions to the proton spin have been mounted at three laboratories. There is the COMPASS experiment at CERN, experiments from the RHIC Spin group at the Relativistic Heavy Ion Collider (RHIC) at Brookhaven, and the HERMES experiment at HERA. We will discuss particularly the COMPASS experiment.

At COMPASS, the goal was to measure gluon contributions to the proton spin through photon-gluon fusion.[40] In this process, shown schematically in Fig. 14, a polarized muon beam couples to a virtual photon. This in turn is coupled to the polarized gluon distribution in the proton through production of a quark-antiquark pair. The final scattered muon is observed in coincidence with a final hadronic state which has strong overlap with the $q - \bar{q}$ pair. The COMPASS experiment focused on two different hadronic states; the first was 'open charm,' observation of a final-state hadron containing a charm quark. The second situation involved two final-state hadrons with large transverse momentum p_T.

The right-hand side of Fig. 14 shows measurements of $\Delta g(x)/g(x)$ from several laboratories.[41] The star represents the COMPASS open-charm measurement.
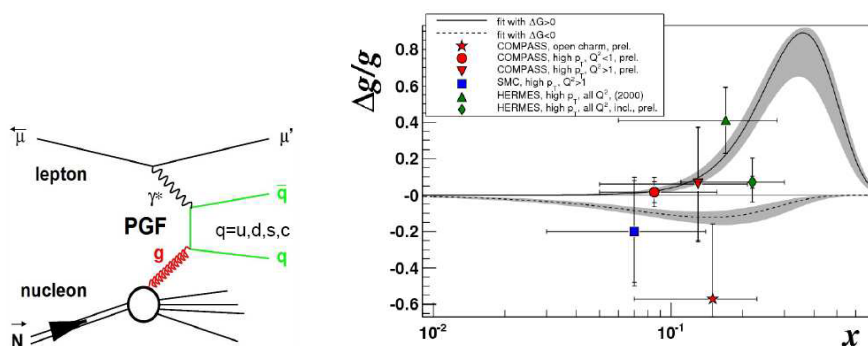
Fig. 14. Left: schematic diagram illustrating 'photon-gluon fusion.' The virtual photon from a polarized muon couples to the gluon distribution through production of a quark-antiquark pair. Right: $\Delta g(x)/g(x)$ vs. x. Star: COMPASS open-charm measurement; circle and downward-facing triangle: COMPASS high-p_T measurements with different Q^2 cuts; square: SMC high-p_T measurement; upward-facing triangle and diamond: two different HERMES high-p_T measurements.

The circle and downward-facing triangle are COMPASS high-p_T measurements corresponding to different Q^2 cuts. The square is a high-p_T measurement from the Spin Muon Collaboration (SMC) group. The upward-facing triangle and the diamond are two different HERMES high-p_T measurements. The data is all for values $0.05 < x \leq 0.2$. The values of $\Delta g(x)/g(x)$ are all small and in most cases the errors in both Δg and the average value of x are relatively large. The errors are sufficiently large that the sign of Δg is not clear. The two curves show fits to these data with $\Delta G > 0$ and $\Delta G < 0$.

If one takes the COMPASS values one obtains for the total gluon contribution to the proton spin, $\Delta G/G = -0.57 \pm 0.41 \ (stat) \pm 0.17 \ (syst)$ for the open charm measurements, and $\Delta G/G = 0.016 \pm 0.058 \ (stat) \pm 0.0055 \ (syst)$ for the high-p_T measurements.[42] Combining the COMPASS measurements with the SMC, HERMES and RHIC spin results, the best value of ΔG is small; however, it is still statistically possible that ΔG could be large. Fig. 14 does not show RHIC spin results that give comparable values for $\Delta G/G$ in a similar x region.

6.3.3. *Current status of the proton spin question*

At the present time, despite the large errors on the gluon contribution to the proton's spin, it appears that polarized gluons are unlikely to carry the majority of the proton's spin. We are left with the question of just what fraction of the spin of the proton is carried by polarized glue, or by quark or gluon orbital momentum. An area that is being pursued at the moment is hard exclusive processes, such as deeply virtual Compton scattering or DVCS (where a charged lepton interacting with a nucleon exchanges a virtual photon with high Q^2, producing a real photon in the final state), or exclusive meson production in lepton-nucleon scattering. These processes can be described in terms of so-called generalized parton distributions or

GPDs. It was shown by Ji that a particular moment of the GPDs could be related to the total orbital angular momentum of the quarks.[43]

Investigations of DVCS have been undertaken at HERA and at Jefferson Laboratory. A major focus of the 12 GeV upgrade at Jefferson Lab will be studies of DVCS and exclusive meson production. The physics of the 12 GeV upgrade will be reviewed in detail in the first lecture by Tony Thomas at this workshop.[44] Thomas' second lecture will summarize his recent work with Myrher on the spin of the proton, which will address the questions raised in this section.

7. New and Proposed Facilities to Study Nucleon Structure

To date, much information on the partonic structure of the nucleon has been obtained from a series of high-energy machines. The first experiments that showed scaling in high-energy deep inelastic scattering were carried out at SLAC. Following these measurements were continuing fixed-target experiments at SLAC, and both fixed-target and collider studies at CERN and Fermilab. The HERA asymmetric electron-proton collider proved to be a nearly ideal facility to map out parton distributions over a very wide range of x and Q^2. Neutrino and antineutrino beams at Fermilab and CERN allowed one to separate out contributions from different quark flavors. Studies of Drell-Yan processes at Fermilab and CERN provide processes sensitive to sea quark distributions in the nucleon.

Now that HERA has ceased operations, experiments at CERN and Fermilab continue. Various new facilities or upgrades of existing ones have the capability of extending our knowledge regarding the partonic structure of the nucleon. The first is the Large Hadron Collider or LHC which will very shortly begin operation at CERN. The primary thrust of LHC operations will be first to find the Higgs particle, a new massive particle which is predicted to appear as the result of the spontaneous breaking of electroweak symmetry. Next, the LHC will focus on discovering either supersymmetric particles or other new phenomena beyond the Standard Model. However, the LHC also could have potential applications in determining the partonic content of hadrons.

There are also several new facilities, or upgrades of existing facilities, which could examine the partonic content of hadrons. Here I will discuss one upgrade of an existing facility and one proposed new facility in this regard. The first, the upgrade of the electron accelerator at Thomas Jefferson Laboratory, is the subject of the first lecture by Tony Thomas at this workshop.[44] As a result, I will provide only a brief summary of this project; I refer the reader to his talk on this subject. The second is a proposed new electron-ion collider. Two possible versions of this machine have been suggested, one which would be located at Brookhaven National Laboratory and a second which would be the subject of a future upgrade at Jefferson Laboratory.

I will very briefly discuss the 12 GeV upgrade of the CEBAF accelerator at Thomas Jefferson National Laboratory.[45] The upgrade will provide 12 GeV con-

tinuous electron beams to a new Hall D experimental area, which will produce real photon beams that should provide precision spectroscopy. This should help to study possible 'exotic' states, particularly excited mesons that contain one or more gluons. In addition, the upgrade would provide up to 11 GeV beams to the existing halls A, B and C.

As was mentioned in the preceding section, a major focus of effort following the Jefferson Lab upgrade would be on hard exclusive processes such as DVCS or exclusive meson production. It has been shown that these hard exclusive processes can be described in terms of integrals over quark distributions. These are termed 'generalized parton distributions' or GPDs. GPDs can provide information regarding the longitudinal momentum and transverse position of quarks in the nucleon, and could test the Ji sum rule.[43] Following the upgrade, Jefferson Lab will have unique kinematic capabilities. It will be able to access parton distributions in regions of x and Q^2 that complement those accessible at laboratories like CERN or HERA. In particular, after the upgrade Jefferson Lab will be able to reach regions of Bjorken $x \sim 0.6$ and values $Q^2 \sim 8$ GeV^2.

A proposed new facility is an electron-ion collider. This would consist of an electron beam colliding with either light ions or heavy ions. Plans to date call for achieving a value $s = 20-100\,\text{GeV}^2$, with high luminosity. There are two suggestions for such a facility.[46] In each case this would involve building a new accelerator to complement an existing machine. The first case would involve building an electron ring at Brookhaven, to collide with hadrons from the current RHIC facility. The left-hand side of Fig. 15 shows a schematic picture of such a facility. A proposed electron ring would be added to the RHIC complex at Brookhaven; the ring would
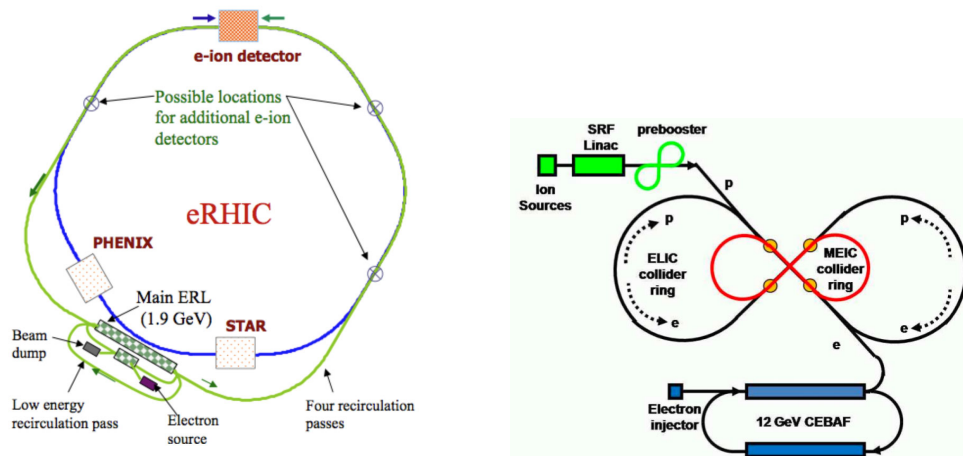

Fig. 15. Conceptions of possible electron-ion colliders. Left: eRHIC. An electron ring added to the RHIC complex at BNL. Right: electron-light ion collider at Jefferson Lab. A hadron ring would be added to the CEBAF accelerator, accelerating protons and light ions.

provide electrons with energies in the range 5-10 GeV, with the possibility of a recirculating linac injector. The electrons would collide with beams of heavy or light ions from the RHIC accelerator.

The second scenario would involve building a light ion accelerator at Jefferson National Laboratory. This would produce hadrons of 50-100 GeV, to collide with electrons of roughly 5 GeV from CEBAF. The right-hand side of Fig. 15 shows a schematic picture of such a facility. A hadron ring (in this diagram, shown in a figure-eight configuration) would be added to the CEBAF electron accelerator at Jefferson Lab. The ring would provide protons and light ions with energies in the range 50-100 GeV. The proposed hadron accelerator would feature four intersection points. Present estimates suggest that very high luminosities ($\mathcal{L} \sim 10^{34}/\text{cm}^2 \cdot \text{sec}$) might be achieved in such a collider.

With an electron-ion collider one could provide quantitative measurements of quark spins through semi-inclusive DIS. It would have the possibility of measuring PDFs (and particularly gluon distributions) at very small Bjorken x. Gluon probabilities in the nucleon increase extremely rapidly at very small x values, as can be seen from Fig. 11. The large nucleon densities in the center of the nucleus could in principle support extremely large gluon densities. If gluon distributions continue to increase in the interior of the nucleus, at some point nuclear gluon probabilities would exceed the unitarity bound. Thus one expects at some point for many-body effects to slow down this increase. Some have suggested that this will lead to a qualitatively new cooperative effect termed a 'color-glass condensate'.[47] An electron-ion collider, particularly eRHIC which supports heavy-ion hadronic beams, would be able to probe this dynamical region.

An electron-ion collider would also have the capabilities of exploring generalized parton distributions over a fairly wide kinematic region. Such colliders could also provide detailed quantitative studies of the structure of mesons, particularly pions. One other area that could be studied with an electron-ion collider is the process of fragmentation. This is the process whereby a quark produces a final hadron. Possible kinematics for electron-ion colliders would have the capability of exploring both beam fragmentation and the so-called target fragmentation regions.

Acknowledgments

References

1. A review of accelerator and detector development with many fine images is Frank Close, Michael Marten and Christine Sutton, *The Particle Odyssey* (Oxford University Press, Oxford 2002).
2. W.-M. Yao *et al.*, (Particle Data Group) *J. Phys. G* **33** (2006) 1.
3. M. Goldberger and K. M. Watson, *Collision Theory* (Wiley and Sons, New York 1964).

4. G. Breit and E. Wigner, *Phys. Rev.* **51** (1937) 593.
5. M. Boglione and M. R. Pennington, *Phys. Rev. D* **65** (2002) 114010.
6. R. H. Dalitz, *Phys. Rev.* **94** (1954) 1046.
7. C. Amsler *et al.*, *Eur. Phys. J. C* **23** (2002) 29.
8. M. Gell-Mann and Y. Ne'eman, *The Eightfold Way* (W. A. Benjamin, New York 1964).
9. P. E. Schlein *et al.*, *Phys. Rev. Lett.* **11** (1963) 167.
10. V. E. Barnes *et al.*, *Phys. Rev. Lett.* **12** (1964) 204.
11. M. Gell-Mann, *Phys. Lett.* **8** (1964) 214.
12. G. Zweig, CERN preprint 8182/TH401 (1964) unpublished.
13. F. E. Close, *An Introduction to Quarks and Partons*, (Academic Press, New York 1979).
14. L. W. Jones, *Rev. Mod. Phys.* **49** (1977) 717.
15. O. W. Greenberg, *Phys. Rev. Lett.* **13** (1964) 598; M. Y. Han and Yoichiro Nambu, *Phys. Rev.* **129** (1965) B1006.
16. L. Hoddeson, L. M. Brown, M. Riordan and M. Dresden, *The Rise of the Standard Model: Particle Physics in the 1960s and 1970s* (Cambridge University Press, 1997).
17. J. J. Aubert *et al.*, *Phys. Rev. Lett.* **33** (1974) 1404; J. E. Augustin *et al.*, ibid. p. 1406.
18. S. W. Herb *et al.*, *Phys. Rev. Lett.* **39** (1977) 252.
19. F. Abe *et al.*, *Phys. Rev. Lett.* **74** (1995) 2626.
20. Nathan Isgur and Mark B. Wise, *Phys. Lett. B* **232** (1989) 113; *Phys. Lett. B* **237** (1990) 527.
21. R. K. Ellis, W. J. Stirling and B. R. Webber, *QCD and Collider Physics* (Cambridge University Press, 1996).
22. D. J. Gross and Frank Wilczek, *Phys. Rev. Lett.* **30** (1973) 1343; H. D. Politzer, *ibid.* 1346.
23. G. Sterman *et al.*, *Rev. Mod. Phys.* **67** (1995) 157.
24. L. W. Whitlow *et al.*, (SLAC), *Phys. Lett. B* **282** (1992) 475; C. J. Adloff *et al.*, (H1), *Eur. Phys. J. C* **21** (2001) 33; S. Chekanov *et al.*, (ZEUS), *Eur. Phys. J. C* **21** (2001) 443; A. C. Benvenuti *et al.*, (BCDMS), *Phys. Lett. B* **223** (1989) 485; M. Arneodo *et al.*, (NMC), *Nucl. Phys. B* **483** (1997) 3; M. R. Adams *et al.*, (E665), *Phys. Rev. C* **54** (1996) 3006.
25. E. D. Bloom *et al.*, *Phys. Rev. Lett.* **23** (1969) 930; M. Breidenbach *et al.*, ibid. p. 935.
26. J. Ashman *et al.*, (EMC), *Nucl. Phys. B* **328** (1989) 1; P. L. Anthony *et al.*, (E142) *Phys. Rev. D* **54** (1996) 6620; K. Abe *et al.*, (E143) *Phys. Rev. D* **58** (1998) 112003; B. Adeva *et al.*, (SMC) *Phys. Rev. D* **60** (2000) 072004; A. Airepetian *et al.*, (HERMES) *Phys. Lett. B* **442** (1998) 484; K. Abe *et al.*, (E154) *Phys. Rev. Lett.* **70** (1997) 26; P. L. Anthony *et al.*, (E155) *Phys. Lett. B* **493** (2000) 19.
27. Yu. L. Dokshitzer, *Sov. Phys. JETP* **46** (1977) 641; V. N. Gribov and L. N. Lipatov, *Sov. J. Nucl. Phys.* **15** (1972) 438; G. Altarelli and G. Parisi, *Nucl. Phys. B* **126** (1977) 287.
28. S. D. Drell and T.-M. Yan, *Phys. Rev. Lett.* **25** (1970) 316.
29. D. Mason, *Proceedings of the 14th International Workshop on Deep Inelastic Scattering (DIS06)*, ed. M. Kuze, K. Nagano and K. Tokoshuku (World Scientific Press, Singapore 2007), p. 165.
30. J. R. Pumplin *et al.*, (CTEQ), *Jour. High Energy Phys.* **0202** (2002) 012.
31. A. D. Martin *et al.*, (MRST), *Eur. Phys. J. C* **35** (2004) 325.
32. J. Speth and A. W. Thomas, *Adv. Nuc. Phys.* **24** (1997) 83.
33. J. T. Londergan and A. W. Thomas, *Prog. Part. Nuc. Phys.* **41** (1998) 49.

34. M. Arneodo, *Phys. Rept.* **240** (1994) 301.
35. D. F. Geesaman, K. Saito and A. W. Thomas, *Annu. Rev. Nucl. Part. Sci.* **45** (1995) 337.
36. V. N. Gribov, arXiv:hep-ph/0006158; V. A. Abramovsky, V. N. Gribov and O. V. Kancheli, *Sov. J. Nucl. Phys.* **18** (1974) 308.
37. S. A. Kulagin and R. Petti, *Nucl. Phys. A* **765** (2006) 126.
38. B. Adeva *et al.*, (SMC), *Phys. Lett. B* **420** (1998) 180; K. Ackerstaff *et al.*, (HERMES), *Phys. Lett. B* **464** (1999) 123.
39. E. Leader and M. Anselmino, *Z. Phys. C* **41** (1998) 239.
40. F. Bradamante, *Prog. Part. Nucl. Phys.* **55** (2005) 270.
41. V. Yu Alexakhin *et al.* (COMPASS), *Phys. Lett. B* **647** (2007) 8; B. Adeva *et al.* (SMC), *Phys. Rev. D* **60** (1999) 072004; A. Airapetian *et al.* (HERMES), *Phys. Rev. D* **75** (2007) 012007.
42. E. S. Ageev *et al.* (COMPASS), *Phys. Lett. B* **647** (2007) 330.
43. X. D. Ji, *Phys. Rev. Lett.* **78** (1997) 610.
44. A. W. Thomas, proceedings of this workshop, *Int. J. Mod. Phys. E* **18** (2009) 1116.
45. The Science and Experimental Equipment for the 12 GeV Upgrade of CEBAF, http://www.jlab.org/12GeV/development.html.
46. A. Deshpande, R. Milner, R. Venugopalan and W. Vogelsang, *Ann. Rev. Nucl. Part. Sci.* **55** (2005) 165.
47. L. D. McLerran and R. Venugopalan, *Phys. Rev. D* **49** (1994) 2233; *ibid.* p. 3352.